IEEE Access
Multidisciplinary ⋮ Rapid Review ⋮ Open Access Journal

Received 19 January 2024, accepted 27 January 2024, date of publication 13 February 2024, date of current version 27 February 2024.

Digital Object Identifier 10.1109/ACCESS.2024.3365489

RESEARCH ARTICLE

Non-Uniform Background Noise Suppression Method Based on Improved Total Variation Model for Wide-Field Imaging System

PENGJI ZHOU[1,2], DI WU[1], XIAODONG WANG[1], CHANGXIANG YAN[1], AND DALI ZHOU[1]
[1]Changchun Institute of Optics, Fine Mechanics and Physics, Chinese Academy of Sciences, Changchun 130033, China
[2]University of Chinese Academy of Sciences, Beijing 100049, China

Corresponding author: Di Wu (wudi@ciomp.ac.cn)

This work was supported by the Strategic Priority Research Program of Chinese Academy of Sciences under Grant XDA17010205.

ABSTRACT A wide-field surveillance system with a long exposure time has a stronger detectability for dim space targets. However, with the increase in exposure time and working temperature, complex non-uniform background noise containing hot pixels of the detector cannot be ignored, seriously affecting the background and imaging quality. This article studies and proposes a high-performance denoising method, which does not use any prior knowledge of the target and can automatically remove noise from the image. This method is based on an improved total variation model to remove hot pixels and other background mixed noise in wide-field system images. Firstly, using the idea of the traditional local contrast method (LCM), we utilize the significant difference in grayscale values between contaminated pixels and neighboring pixels to detect impulse noise, such as the hot pixels in the image. And then, we designed an improved adaptive maximum filtering algorithm to remove unwanted contamination, which protected target information from being lost and optimized pixels that were attacked by impulse noise. Finally, the total variation algorithm is used to eliminate residual background noise, the detector's readout noise, and non-uniform response. The method proposed in this article can effectively filter out hot pixels and non-uniform background noise while preserving the details of target edges. We conducted experiments on a large number of simulated and original images. For star maps captured in long exposure mode, the method proposed in this article has obvious advantages over several competing algorithms. The experimental results show that, compared to competitive algorithms, the algorithm proposed in this article improves PSNR by at least 13.1%, SSIM by at least 0.4%, IEF by at least 5 times, and IQI by at least 9.2%. At the same time, the algorithm in this article achieved a moderate level of computation time.

INDEX TERMS Wide-field surveillance system, long exposure time, non-uniform correction, local contrast method, maximum filter, total variation.

I. INTRODUCTION

In the past decade, the number of space debris has sharply increased [1], [2]. The continuous entry of small launch vehicles and large constellations into orbit has led to a high density of space orbiters, exacerbating the space situation, such as anti-satellite weapon testing, in-orbit collisions, and satellite explosions [3]. The main purpose of space surveillance is to accurately identify and locate space targets, which is an important component of space situational awareness and an important technical guarantee for ensuring the safety of manned spaceflight [4], [5]. Due to the long distance, weak energy, and often accompanied by a large amount of background noise of the observed target signals [6], higher requirements are placed on the detection ability of existing surveillance systems. The far imaging distance makes the target appear weaker on the image plane, occupying only a few pixels and without features such as contours, textures, and shapes. Meanwhile, due to the influence of spatial clutter, targets are often submerged in

The associate editor coordinating the review of this manuscript and approving it for publication was Wei Liu.

the background, and the interference of system noise makes the detection of weak targets very difficult. In addition, both CCD and CMOS detectors contain inherent non-uniform noise. Therefore, to improve the detection ability of dim targets in space, wide-field surveillance systems often adopt a long exposure time mode to obtain more energy from the target. Wide-field surveillance systems will obtain a large number of such images for scientific research. However, as the exposure time of the detector increases, it can cause a large amount of hot pixels [7]. which will seriously affect the quality of the star map and be detrimental to space science applications. At the same time, in the long exposure mode, the Photo Response Non-Uniformity (PRNU) of the detectors also has a destructive effect on the image. Furthermore, if the background is moving, the energy concentration is low and target extraction becomes more difficult [8], [9]. Therefore, it is necessary to denoise the images of the wide-field imaging system to improve the system's ability to detect spatial targets, and at the same time, it plays a crucial role in obtaining high-quality spatial remote sensing images. So, Noise removal or denoising is a post-processing task for image-related applications.

Background non-uniformity is the main interference factor that suppresses detection ability. Background non-uniformity is mainly caused by two aspects: one is the non-uniformity of the detector's focal plane caused by the detector's performance, and the other is caused by complex background noise. Therefore, in recent years, many methods for suppressing background non-uniformity have been proposed. These methods can be summarized into two main categories: calibration-based methods and scene-based methods [10]. The calibration-based methods have the characteristics of simple calculation and high correction accuracy and are widely used in engineering. Traditional non-uniform correction experiments are related experiments conducted on the ground before spacecraft launch, which have the characteristics of high correction accuracy and easy operation. To some extent, this category of methods can overcome the non-uniformity of the response between pixels of the detector itself [11], [12], [13]. However, after the aircraft is launched and put into orbit for some time, the performance of the detector will decay, and the parameters obtained from previous ground calibration tests may no longer be applicable. However, as the working time of the detector increases, the temperature drift and time drift of the detector will make the correction parameters no longer applicable in the complex spatial target background. Therefore, the non-uniform correction coefficients, obtained from radiation calibration experiments conducted before the practical application of wide-field monitoring systems, may not be applicable as the working time increases on orbit. The scene-based method estimates noise based on the difference between the target and the background, without considering temporal correlation. It is mainly divided into two main categories, one is based on filtering methods, and another is based on model-driven and learning methods. Although the latter has made some progress [14], [15], the time complexity of this category needs to be reduced. The spatial targets of the wide-field imaging system are all point targets without texture, motion, and other features, making it difficult to obtain target characteristics through learning methods. Meanwhile, the image needs to undergo denoising in orbit, which requires a simple algorithm and implementation on embedded hardware such as FPGA. Therefore, this type of method is not applicable. There are two main processing methods, frequency domain filtering and spatial domain filtering. The typical methods of frequency domain filtering include Fourier transform denoising and wavelet transform denoising. The idea is to transform the spatial image into the frequency domain, use the characteristics of noise in the frequency domain for threshold segmentation, and convert the processed frequency domain information into the spatial domain image, which can achieve the purpose of removing noise [16], [17], [18]. However, although frequency domain filtering can eliminate noise, it can also cause certain distortion of the target. For images with a star background, the edge of the target after the frequency domain is filtered is prone to oscillation. Spatial filtering is a neighborhood processing method that directly processes pixels within the neighborhood in the image space to achieve the effect of smoothing or sharpening the image [19]. Typical spatial filtering algorithms include median filtering algorithm (MF) [20], [21], [22], bilateral filtering algorithm (BF) [23], [24], non-local mean filtering algorithm (NL-means) [25], and image denoising algorithm based on partial differential equations [26], etc. The above methods have good background noise suppression capabilities in different fields, but these algorithms are sensitive to complex background noise and the denoising effect is not ideal.

The noise studied in this article includes two types: the hot pixels that cannot be ignored under long exposure, and non-uniform background noise in spatial images. Due to thermal excitation, the photoelectricity detector still has a current output under the dark field condition, which is called dark current, it is the main reason for generating hot pixels. The non-uniform background noise in this article refers to the sum of reset noise and amplifier noise generated by electrons during the readout processing [27]. However, impulse noise such as the hot pixels is discrete and has a large amplitude in the image, with only a single pixel in the spatial domain. To overcome the shortcomings of the above methods in suppressing complex background noise in spatial environments, this paper proposes a high-precision and robust background noise removal method based on the total variation denoising model, which is an enhanced total variation algorithm based on local contrast maximum filtering (LCMF-TV). Traditional total variation algorithms have certain limitations in effectively removing hot pixels from complex background noise. Therefore, based on the traditional total variation denoising model and inspired by the local contrast algorithm, this algorithm can detect and remove hot pixels in the image. Specifically, the first step is the image

TABLE 1. Parameters of the wide-field surveillance system.

Parameters	Value
Number of detectors	8
Size of per detector	6144×6144
Pixel size	10μm×10μm
Read Noise	4.5e-
Exposure time	3s
Optical system form	Concentric lens group

preprocessing stage, during which an improved adaptive maximum filtering algorithm is designed to accurately estimate and replace pixels attacked by pulse noise. At this step, this algorithm is based on the traditional local contrast algorithm (LCM), targeting the characteristics of pulse noise in long exposure images, namely the significant difference between pulse noise and neighboring pixel grayscale values. A contrast image is established, and an adaptive threshold is used to search and detect pulse noise. Finally, to preserve spatial target information to the greatest extent possible, the maximum value filtering algorithm is used to filter out the pulse noise. The second step is the stage of suppressing non-uniform background noise in the image. In this stage, the image is finally processed based on a total variation model. The total variation model is an anisotropic model that relies on gradient descent to smooth the image, which can preserve the edge information of the target while smoothing the image background. Therefore, the preprocessed image can be further processed to eliminate residual background noise, detector readout noise, etc., and the background can be smoothed.

The content of this article is arranged as follows: Section I introduces the research background of this article, Section II conducts imaging modeling based on the optical image characteristics of wide-field surveillance systems, Section III provides a detailed description of the entire background noise suppression algorithm, Section IV presents experimental results obtained by applying the algorithm through both simulated and real images, and Section V provides conclusions.

II. IMAGING CHARACTERISTICS

The astronomical image data used in the paper was collected by the CMOS wide-field Surveillance System. The specific parameters of the wide-field Surveillance System are listed in Table 1. The wide-field surveillance system adopts an optical system with spherical concentric lenses, uses a fiber optic panel to transmit the imaging plane to the detector's focal plane at the end face, and is spliced with 8 CMOS detectors.

It should be noted that the spatial targets discussed in this article include spatial stars and spatial moving targets. Therefore, based on the characteristics of spatial images, the following model is established [28]:

$$F(i,j) = F_s(i,j) + F_t(i,j) + B(i,j) + N(i,j) \quad (1)$$

where (i,j) is the position of pixels in an image, F represents the captured spatial image, F_s represents spatial star points, F_t represents spatial moving targets, B represents spatial background noise, N represents image noise. Image noise generally includes the non-uniform background of the detector, as well as the readout noise, shot noise, hot pixels, etc.

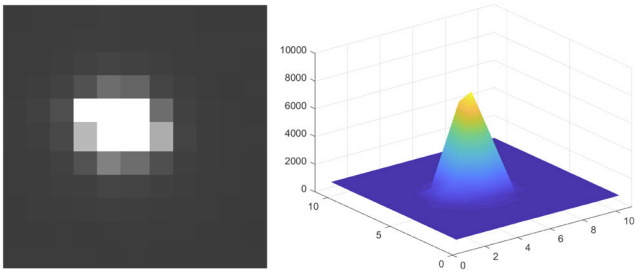

FIGURE 1. (a) Image of a real star; (b) 3D plot of a real star.

Due to sensor hardware limitations, atmospheric interference, and the influence of optical systems, as the Figure 1(b), the grayscale of spatial point targets gradually decreases from the center to the surrounding areas. The imaging of point targets can be approximated by point spread function (PSF) [29]:

$$p(x,y) = A exp\left\{-\frac{1}{2}\left[\frac{(x-x_0)^2}{\sigma_x^2} + \frac{(y-y_0)^2}{\sigma_y^2}\right]\right\} \quad (2)$$

where A is the fixed coefficient, $p(x,y)$ is the grayscale intensity of the image at point (x,y), (x_0,y_0) is the center point of point target imaging, and σ_x and σ_y refer to the horizontal and vertical spread radius of the object, respectively. Ideally, a distant star appears as a symmetrical point source object, i.e. the horizontal spread radius is equal to the vertical spread radius $\sigma_x = \sigma_y$.

In the laboratory, the image and the 3D plot of a real star are shown in Figure 1.

In astronomical observation, there are two ways to improve the detection ability of telescopes or detection systems for dim and small targets. One is to increase the gain of the surveillance system, and the other is to increase the exposure time of the detector. The former method not only enhances dim targets but also amplifies background clutter and noise, including detector readout noise and shot noise. The actual signal-to-noise ratio of the image has not been effectively improved. The latter method can increase the number of target conversion charges, which in turn increases the brightness of the target in the image, thereby improving the signal-to-noise ratio. Therefore, when applied to weak and small target detection in low illumination backgrounds, a long exposure time method is often used. However, a longer exposure time can also increase the hot pixels in the image, seriously interfering with the detection of spatial targets. As shown in Figure 2, it is a spatial real image with the 3s long exposure mode.

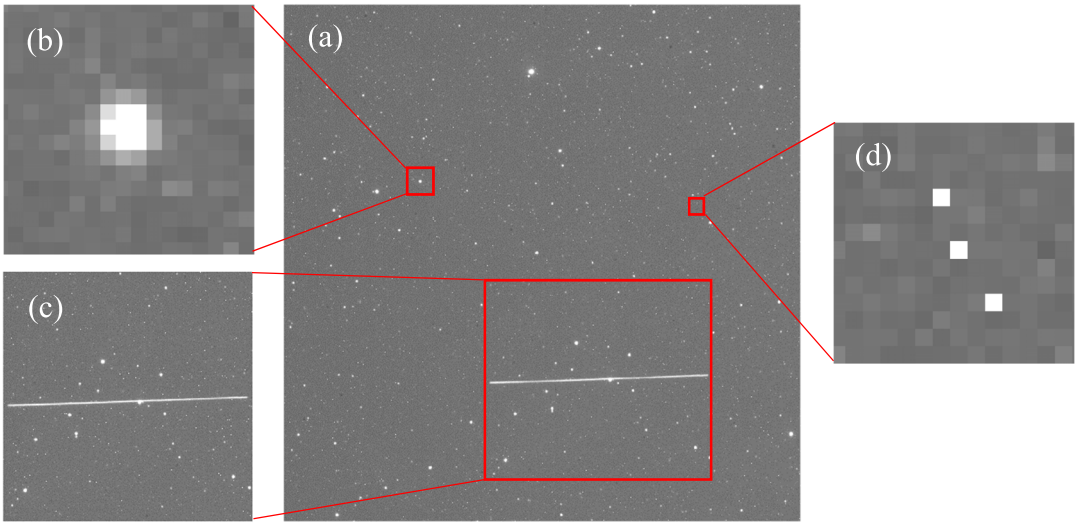

FIGURE 2. (a) Image captured by wide-field Surveillance System; (b) Local area of the stellar-target image; (c) Local area of the moving-target image; (d) Local area of the hot pixels image with long exposure mode.

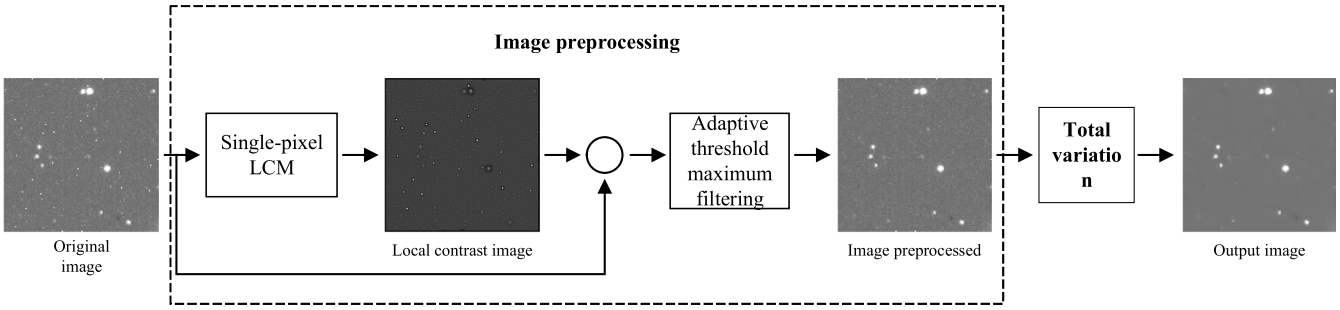

FIGURE 3. Flowchart of the proposed LCMF-TV method.

III. ENHANCED TOTAL VARIATIONAL DENOISING ALGORITHM

Based on the above analysis of wide-field surveillance system imaging, the schematic diagram of the complex background noise suppression algorithm proposed in this article is shown in Figure 3.

A. IMAGE PREPROCESSING

The noise of the original image includes inherent non-uniform noise of the detector, readout noise, hot pixels, etc. Wherein, the inherent non-uniformity problem of detectors can generally be corrected by measuring the correction parameters through non-uniformity correction experiments in the laboratory. And nowadays, the readout noise of the detector is well controlled with the improvement of the detector technology. For the hot pixels, an effective suppression method is to reduce the exposure time of the detector. However, to improve the detection ability and facilitate the observation of weak energy stars or moving targets, the detector needs to adopt a long exposure mode. Therefore, how to effectively suppress the hot pixels of the detector in long exposure mode will be beneficial for improving image quality.

Under ideal conditions, when there is no light irradiation, the photodetector should have no photocurrent output. However, in reality, due to thermal excitation, impurities, and defects inside the material, in the absence of light, the photodetector still has a current output, which is called dark current [30]. This is the main reason for hot pixels. Due to the random nature of the various excitation conditions mentioned above, the hot pixels also fluctuate randomly.

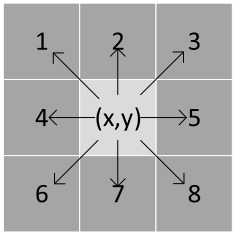

FIGURE 4. Pixel attacked by hot pixel compared with 8-Neighborhood.

According to the characteristics of the human visual system, the hot pixels in the long exposure mode are significantly different from other pixels in the 8-neighborhood, as shown in Figure 4.

According to the above analysis, we propose an algorithm called adaptive maximum filtering algorithm based on local contrast.

Calculate the local contrast of each pixel in an image using the following formula (Single-pixel LCM) [31].

$$c(x,y) = \frac{I(x,y)}{M(x,y)} \tag{3}$$

$$M(x,y) = \frac{\sum_{i=1}^{8} m_i}{8} \tag{4}$$

where $c(x,y)$ represents the local contrast of a single pixel at point (x,y) in the image, $I(x,y)$ represents the grayscale value, $M(x,y)$ represents the grayscale mean of the 8-neighborhood, m_i represents the grayscale value of the 8 neighborhoods.

To effectively identify contaminated pixels, an adaptive threshold segmentation method is adopted for the calculated single-pixel local contrast graph $c(x,y)$. Due to the influence of the hot pixels with long exposure times, the grayscale values of contaminated pixels are significantly higher than their 8-neighborhood mean. If the threshold calculated by the mean and standard deviation of the entire image is used for image segmentation, the spatial target will affect the size of the threshold and affect the correct detection of the hot pixels. Therefore, an improved adaptive method based on 8-neighborhood is proposed, the threshold calculation formula is as follows:

$$Th_C = \mu_C + \alpha\sigma_C \tag{5}$$

where μ_C is the mean of local contrast of 8-neighborhood, σ_C is the standard deviation of local contrast in 8 neighborhoods, α is a coefficient, according to the experimental test results, it is generally taken as 1.5.

The mean and standard deviation of the 8-neighborhood local contrast of (x,y) pixel can be expressed as:

$$\mu_C = \frac{1}{N}\sum_{i=1}^{N} c_i(x,y) \tag{6}$$

$$\sigma_C = \sqrt{\frac{\sum_{i=1}^{N}\left[c_i(x,y) - \mu_C(x,y)\right]^2}{N-1}} \tag{7}$$

where c_i represents the local contrast of 8-neighboring pixels. Because it is an 8 neighborhood, N here is 8.

After the above analysis, when $c(x,y)$ is greater than the threshold $Th_C(x,y)$, it can be determined that (x,y) is a pixel contaminated by impulse noise such as a hot pixel, and then, this pixel adopts the template of 3×3 for maximum filtering, replacing contaminated pixels with the maximum value of the neighborhood. The purpose of using maximum filtering is to prevent a decrease in structural similarity after image processing. The formula is as follows:

$$SLCM(x,y) = \begin{cases} max\{I(x-k,y-l)\}, (k,l \in W) & c(x,y) > Th(x,y) \\ I(x,y) & c(x,y) \le Th(x,y) \end{cases} \tag{8}$$

where W is the maximum filtering template of 3×3, SLCM represents the processed result at where W is the maximum filtering template of 3×3, SLCM represents the processed result at (x,y).

After the above method of processing, pixels that are not contaminated by hot pixels remain unchanged, and the contaminated pixels are processed by improved maximum filtering to obtain the final processing result. Due to only operating on the neighborhood of the detected hot pixel and not involving other pixel points in the calculation, the possibility of artifacts in the image is greatly reduced Using an adaptive maximum algorithm based on local contrast (LCMF), the image and its grayscale 3D image before and after filtering are shown in Figure 5.

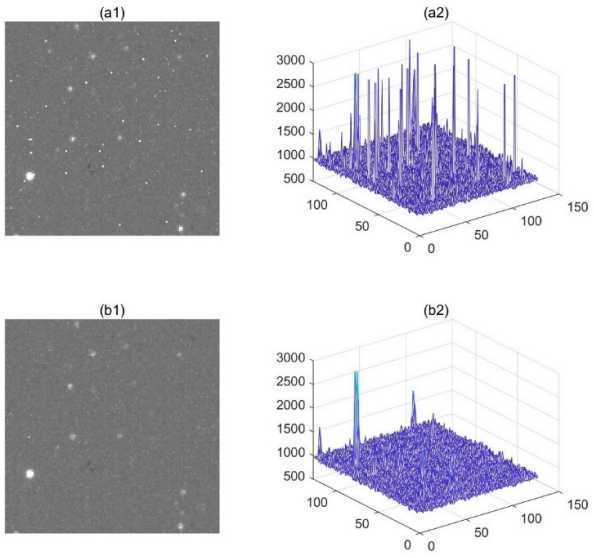

FIGURE 5. (a1) and (b1) represent the original image and the image after improved maximum filtering, respectively. (a2) and (b2) represent the grayscale three-dimensional images of the corresponding image data.

Algorithm 1 is the pseudocode of the LCMF algorithm.

Algorithm 1 Adaptive Maximum Filtering Algorithm Based on Local Contrast (LCMF)

Input: The original image I of wide-field surveillance

1. Calculate matrix M using formula (4).
2. Calculate matrix C using formula (3).
3. Calculate variable 'MeanC' using the formula (6).
4. Calculate variable 'SdC' using the formula (7).
5. Calculate variable 'Th' using formula (5).
6. if C(i,j)>Th,
   O(i,j) = max(8-neighborhood pixels of I(i,j)).
   else
   O(i,j) = I(i,j)
   end

Output: Image O processed by algorithm.

B. TOTAL VARIATION

After applying the algorithm proposed in the previous section to the original image, most of the hot pixels

caused by long exposure were filtered out, but a portion of the background clutter noise was still retained, and its probability density function approximately follows a standard normal distribution. To eliminate this part of the noise, a total variation method (TV) was used. TV is a constrained optimization numerical algorithm used to remove image noise, which minimizes the total variation of the image for denoising. Using Lagrange multipliers to impose constraints and using gradient projection algorithm to solve. The difference between adjacent pixels in the low-frequency part of the image is small, and the total variation method can smooth the image in that part; The high-frequency part of the image is the contour edge, and the total variation method does not perform smoothing in this part, preserving the image edge information [32]. The numerical algorithm is simple, fast, and suitable for background noise removal.

After image preprocessing, the grayscale values of the image can be represented as follows:

$$\bar{f}(x,y) = f(x,y) + n(x,y) \tag{9}$$

where $\bar{f}(x,y)$ represents the preprocessed image of the original image, $f(x,y)$ represents the clean image that has not been contaminated, and $n(x,y)$ represents the residual noise in the image. As described previously, this noise approximately follows a standard normal distribution.

To obtain the restored image $f(x,y)$, we use the total variation method to establish the following constraint equation [33]:

$$\begin{aligned} &min\, E\left[f_0(x,y)\right] \\ &= \iint \left|\nabla f(x,y)\right| dxdy + \frac{\lambda}{2}\iint \left[\bar{f}(x,y) - f(x,y)\right]^2 dxdy \\ &= \iint \left\{\left|\nabla f(x,y)\right| + \frac{\lambda}{2}\left[\bar{f}(x,y) - f(x,y)\right]^2\right\} dxdy \end{aligned} \tag{10}$$

where $\frac{1}{2}\iint \left[\bar{f}(x,y) - f(x,y)\right]^2 dxdy$ is a loss function, it mainly plays a role in preserving the original image characteristics and reducing image distortion. $\iint \left|\nabla f(x,y)\right| dxdy$ is total variational term, λ is the regularization coefficient, it plays an important role in balancing denoising and smoothing, as it depends on the level of noise. t. In the equation, $\left|\nabla f(x,y)\right|$ represents gradient, and calculates according to the following equation:

$$\left|\nabla f(x,y)\right| = \sqrt{\left(\frac{\partial f(x,y)}{\partial x}\right)^2 + \left(\frac{\partial f(x,y)}{\partial y}\right)^2} \tag{11}$$

here, let the function:

$$\begin{aligned} &F\left[x, y, f(x,y), \frac{\partial f(x,y)}{\partial x}, \frac{\partial f(x,y)}{\partial y}\right] \\ &\quad = \frac{\lambda}{2}\left[\bar{f}(x,y) - f(x,y)\right]^2 + \left|\nabla f(x,y)\right| \end{aligned} \tag{12}$$

The necessary condition for obtaining the minimum value of this function is to satisfy the Euler-Lagrange equation. Then, the Euler-Lagrange equation can be established to find the minimum value [34],

$$\frac{\partial F}{\partial f} = \frac{d}{dx}\left(\frac{\partial F}{\partial f_x}\right) + \frac{d}{dy}\left(\frac{\partial F}{\partial f_y}\right) \tag{13}$$

so, by introducing equation (12) into equation (13), it can be concluded that:

$$\lambda\left(f - \bar{f}\right) = \nabla \cdot \left(\frac{\nabla f}{\left|\nabla f\right|}\right) = \frac{f_{xx}f_y^2 - 2f_x f_y f_{xy} + f_{yy}f_x^2}{\left(f_x^2 + f_y^2\right)\sqrt{f_x^2 + f_y^2}} \tag{14}$$

where,

$$\begin{aligned} f_x &= \frac{\partial f(x,y)}{\partial x} \\ f_y &= \frac{\partial f(x,y)}{\partial y} \\ f_{xx} &= \frac{d}{dx}\left(\frac{\partial f(x,y)}{\partial x}\right) \\ f_{yy} &= \frac{d}{dy}\left(\frac{\partial f(x,y)}{\partial y}\right) \\ f_{xy} &= \frac{d}{dy}\left(\frac{\partial f(x,y)}{\partial x}\right) \end{aligned} \tag{15}$$

we record the calculation result of equation (14) as the parameter div,

$$div = \nabla \cdot \left(\frac{\nabla f}{\left|\nabla f\right|}\right) \tag{16}$$

according to equation (14), the smooth model of TV can be obtained by using the gradient descent method [35],

$$\frac{\partial f}{\partial t} = \nabla \cdot \left(\frac{\nabla \mathrm{f}}{\left|\nabla \mathrm{f}\right|}\right) + \lambda\left(\mathrm{f} - \bar{\mathrm{f}}\right) \tag{17}$$

where, t is an introduced time auxiliary parameter, therefore, the following iterative formula can be obtained,

$$\frac{\partial f}{\partial t} = \nabla \cdot \left(\frac{\nabla f}{\left|\nabla f\right|}\right) + \lambda\left(f - \bar{f}\right) \tag{18}$$

where, n represents the number of iterations, f^n represents the image after n iterations, f^{n+1} represents the image after n+1 iterations, t is an introduced time auxiliary parameter. It is used to transform the solving problem of static nonlinear partial differential equations into an iterative process of dynamic partial differential equations. In the final two-dimensional discretization solution, $\Delta t = 1$.

Algorithm 2 is the pseudocode of the TV algorithm.

IV. EXPERIMENTS AND DISCUSSION

To demonstrate the effectiveness of the algorithm proposed in this article, experimental descriptions were conducted using simulated and real images, respectively. Using algorithms to process noisy images constructed from simulated images, and then comparing the processed images with the original images without noise, to verify the effectiveness of the algorithm. Firstly, perform ablation experiments on the algorithm itself to understand its structure. Secondly, multiple

Algorithm 2 Total Variation Method (TV)

Input: The output image f¯ of LCMF

1. Initialization parameters:
   n = 0, $\Delta t = 1, f^0 = \bar{f}$, $div = \nabla \cdot \left(\frac{\nabla f}{|\nabla f|}\right) = 0$
2. for n = 1:100,
   n = n +1,
   calculate f^(n+1) according to equation (18),
   calculate the parameter div according to equations (16) and (17)
   end
3. let $f = f^{100}$,

Output: Image f processed by the algorithm.

competitive algorithms are used to process the simulated noisy images and compare the processing effects of the algorithms. Finally, the superiority of our algorithm in scientific-level spatial applications is verified using real spatial target images.

A. SIMULATION IMAGES

The data used for the simulation image is 128 × 128 size and 14-bit wide grayscale image. Add Gaussian white noise with a variance of 5% to the simulation image to simulate the detector's background noise. In addition, based on the actual background mean of the captured image and the approximate range of the hot pixels, random noise is added with grayscale values ranging from 1000 to 5000 and a probability density of 0.5%.

The simulation experiment is divided into two parts. The first part is to conduct ablation experiments on the algorithm, with the aim of better understanding the functional effects of each part of the algorithm. To better describe the effectiveness of our algorithm, in the second part, we compare it with other traditional background noise suppression algorithms, including median filtering algorithm (MF), bilateral filtering algorithm (BF), non-local mean filtering algorithm (NL means), and our algorithm (LCMF-TV). For the quality evaluation after removing noise using various methods, we adopt two methods: subjective evaluation and objective evaluation. In subjective evaluation, we use to compare the results of various algorithms after removing noise by the human visual system, as well as grayscale distribution maps to intuitively experience. In objective evaluation, we use two indicators: PSNR and SSIM.

1) ABLATION EXPERIMENTS

We conducted ablation research using multiple sets of simulated images to validate the performance of the proposed algorithm for background noise suppression in spatial target images.

The visual effect of one set of images processed by the algorithm is shown in Figure 6. In the ablation experiments, Figure 6(c) is the image obtained through the adaptive maximum filtering algorithm based on local contrast (LCMF). This algorithm effectively removes impulse noise in the image and preserves the edge contour of the target image, but the noise in the image background has not been improved. From Figure 6(d), it can be seen that the background uniformity of the noisy image is improved by using the total variation method, effectively removing background noise in the image. However, pixels contaminated by impulse noise cannot be restored by using the full variation method. Figure 6(e) is an output image processed by the LCMF-TV algorithm (proposed in this article). The algorithm not only effectively eliminates the hot pixels, but also preserves the target well with clear edge contours.

Figure 7 shows the grayscale distribution map processed by the algorithm in the ablation experiment. From the figure, it can be seen that although the image has been restored to a certain extent after only processing with the LCMF algorithm, there are still some fluctuations in the baseline (DN value around 1000). After only being processed by the total variational algorithm (TV), although the fluctuation of the image baseline is small, most of the hot pixels still have a serious impact on the image. However, after the processing of the algorithm in this article (LCMF-TV), the image has been effectively restored. Not only are the hot pixels in the original noisy image effectively removed, but also the fluctuation of the base DN value is consistent with the original noise-less image.

Then, we use RSNR and SSIM separately as objective evaluation indicators for ablation experiments.

PSNR calculates the signal-to-noise ratio in decibels. It is commonly used to evaluate the quality of a refined image relative to the original image. The PSNR value determines the quality of the refined image. The higher the value, the higher the quality, and vice versa. The mathematical formula for PSNR is:

$$PSNR = 20log_{10}\left(\frac{max\,(I)}{\sqrt{MSE}}\right) \tag{19}$$

$$MSE = \frac{1}{mn}\sum_{i=1}^{m}\sum_{j=1}^{n}[I\,(i,j) - K\,(i,j)]^2 \tag{20}$$

in the equation, $I\,(i,j)$ represents the processed image, $K\,(i,j)$ represents the noisy image, $max\,(I)$ represents the maximum possible pixel value in the processed image, and m and n represent the number of row and column pixels in the image.

Structural Similarity (SSIM) is a metric inspired by the Human Visual System (HVS). SSIM evaluates the quality of images based on information such as brightness, contrast, and structure of the compared images. Unlike the above metrics, it believes that the pixel clusters of an image can intuitively reflect the quality of the image. The SSIM ranges from −1 to +1, where −1 means poor and +1 means perfect match. The calculation formula is as follows:

$$SSIM\,(x,y) = \left[l\,(x,y)^{\alpha}\cdot c\,(x,y)^{\beta}\cdot s\,(x,y)^{\gamma}\right] \tag{21}$$

$$l\,(x,y) = \frac{2\mu_x\mu_y + c_1}{\mu_x^2 + \mu_y^2 + c_1}$$

$$c\,(x,y) = \frac{2\sigma_x\sigma_y + c_2}{\sigma_x^2 + \sigma_y^2 + c_2}$$

$$s\,(x,y) = \frac{\sigma_{xy} + c_3}{\sigma_x\sigma_y + c_3} \tag{22}$$

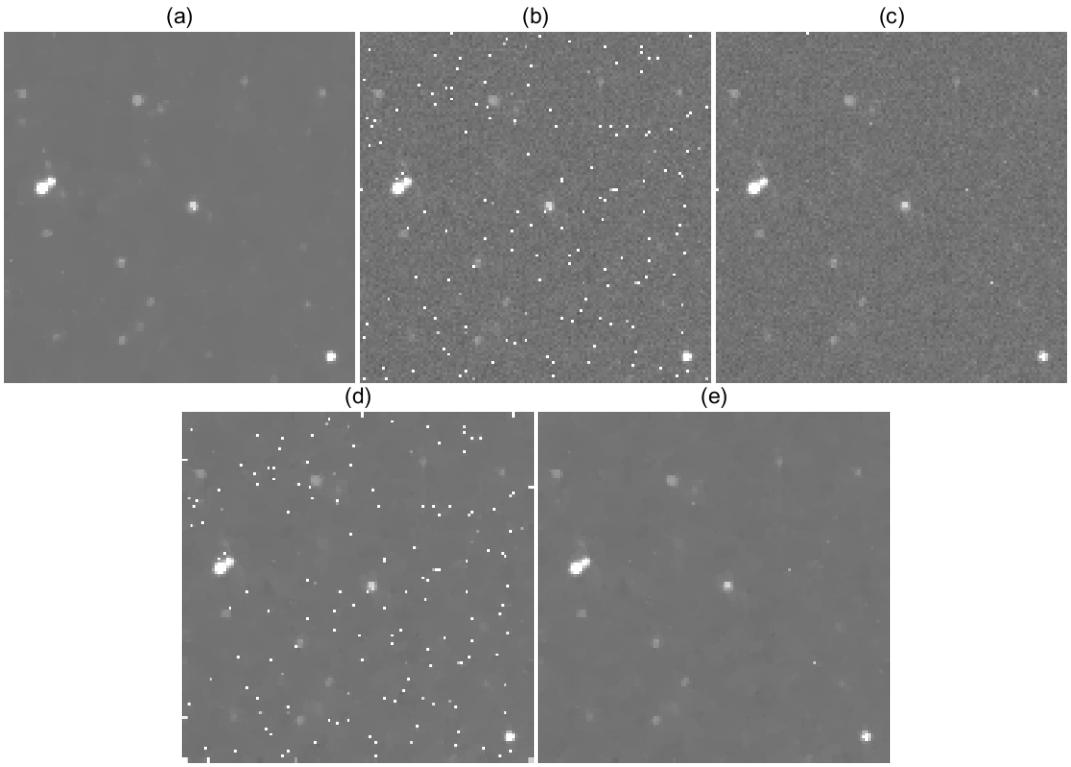

FIGURE 6. Ablation comparative experiment. (a) image without noise. (b) noise image. (c) image processed only by single-pixel LCM. (d) image processed only by TV. (e) image processed by LCMF-TV.

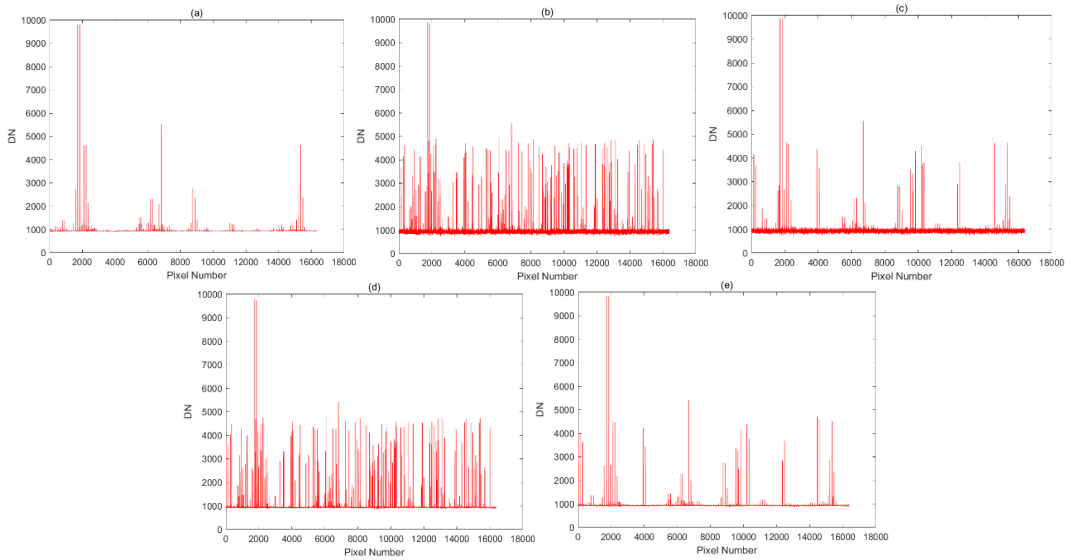

FIGURE 7. Distribution map of grayscale image. (a) distribution map of the image without noise. (b) distribution map of the noise image. (c) distribution map of the image processed only by Single-pixel LCM. (d) distribution map of the image processed only by TV. (e) distribution map of the image processed by LCMF-TV.

in the formula, $l(x, y)$ represents brightness, $c(x, y)$ represents contrast, and $s(x, y)$ represents structure. μ_x is the mean of x, μ_y is the mean of y, σ_x^2 is the variance of x, σ_y^2 is the variance of y, σ_{xy} is the covariance of x and y.

To avoid division by zero, set $c_1 = (k_1 L)^2$ and $c_2 = (k_2 L)^2$, $c_3 = c_2/2$, take $k_1 = 0.01$, $k_2 = 0.03$. L is the maximum pixel value of the image. The selected detector is GSENSE6060 of Gpixel Company, it's each pixel data consists of 14 bits, so L is taken as $2^{14} - 1$. When calculating, we take an N × N window, then continuously sliding the window for calculation, and finally taking the average value as the global SSIM.

TABLE 2. Comparison of test results between PSNR and SSIM in ablation experiments.

Image with noise	LCMF	TV	Imag1		Imag2		Imag3		Imag4		Imag5	
			PSNR	SSIM	PSNR	SSIM	PSNR	SSIM	PSNR	SSIM	PSNR	SSIM
√			37.5286	0.6973	36.4081	0.6446	36.7118	0.6493	36.4205	0.6163	35.9612	0.6362
	√		45.7862	0.9096	44.2447	0.9041	44.2680	0.8969	45.6439	0.9052	43.0603	0.8936
		√	38.0598	0.7595	37.0141	0.7045	37.2284	0.7086	37.0250	0.6739	36.4552	0.6920
	√	√	48.0348	0.9842	47.5441	0.9813	45.9869	0.9695	49.0165	0.9825	44.1732	0.9652

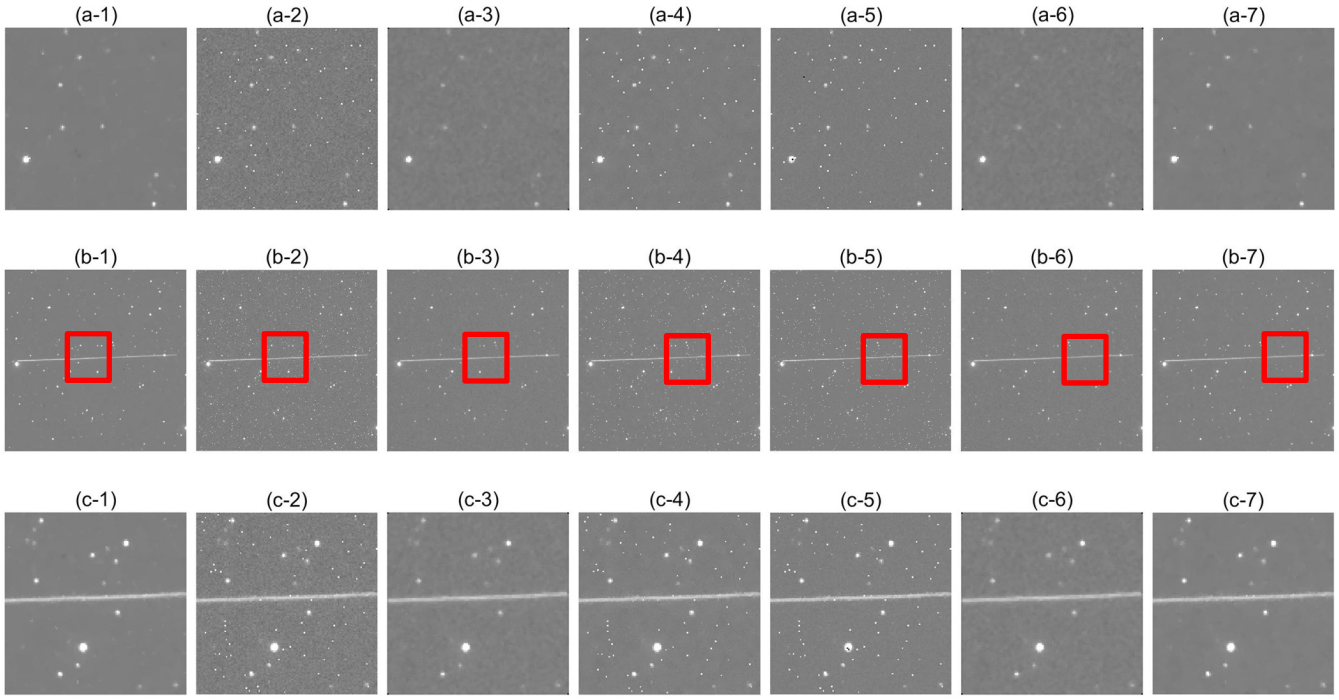

FIGURE 8. The processing effects of various algorithms for simulated images. (a) Simulate star target images. (b) Simulate moving target images(512 × 512). (c) Simulate local detail images of moving targets(128 × 128). (1) image without noise. (2) noise image. (3) MF (4) BF (5) NL-means (6) PDBTMF (7) LCMF-TV.

We calculated PSNR and SSIM according to the above method and recorded the data in Table 2. Five simulated images were selected for analysis in this experiment. From the data in the table, it can be seen that after image processing by using the LCMF algorithm or the TV method, the improvement in PSNR and SSIM is limited. However, after using the LCMF-TV algorithm, taking Imag1 as an example, compared to noisy images, the improvement in PSNR and SSIM is 28.0% and 41.1% respectively. The algorithm proposed in this paper has been fully validated in ablation experiments of simulated images, effectively improving the quality of the images.

2) PERFORMANCE COMPARISON WITH COMPETED METHOD

This section will compare the denoising effects of several classic background noise suppression algorithms in the case of long exposure time of spatial targets, to demonstrate the superiority of our algorithm. These competitive algorithms include a median filtering algorithm (MF), a bilateral filtering algorithm (BF), and non-local mean filtering algorithm (NL-means), and an improved median filtering algorithm (PDBTMF) [36].

a: SUBJECTIVE EVALUATION

Figure 8 shows a visual comparison of the processing results between the four competitive algorithms and the algorithm in this article. Figure (a) shows the image of the star target, Figure (b) shows the image of the moving target, and Figure (c) shows the local detail image of the image of the moving target. Figures (3) to (7) show the processing results of various algorithms on noisy images. It can be seen that Figure (3) effectively removes the impulsive noise in the noisy image, however, there is still a large amount of Gaussian noise in the target background, and the target edge is severely passivated. The Gaussian noise in the target background in Figures (4) and (5) is well suppressed, but the impulse noise in the image cannot be removed. It can be seen that

Figures (6) and (3) exhibit consistent performance, although the PDBTMF is an improved algorithm based on MF, and It has a strong suppression ability for noisy images containing pixels with gray-scale values of 0 or saturation (16383 in this article). However, although the hot pixels in long exposure images cause polluted pixels to be higher than 8 neighboring pixels, it has not reached saturation. Therefore, the PDBTMF algorithm is consistent with the MF algorithm in image processing in this article. Figure (7) clearly shows that after the noise image is processed by the LCMF-TV algorithm, the target details are well preserved, and the background noise is also effectively removed.

b: OBJECTIVE EVALUATION

In objective evaluation, we use four indicators: MSE, PSNR, SSIM, IEF, and IQI to evaluate image quality. Here, IEF refers to the image enhancement factor. IQI refers to the image quality index which is used to evaluate the reconstructed image, it's a quantitative value that indicates the extent of improvement of a reconstructed image [37]

IEF is used to determine the quality of the recovered images and it is termed as the proportion of the distinction between degraded image and input image to the difference between recovered image and original image. The higher the IEF value, the higher the image quality. The calculation formula is as follows.

$$IEF = \frac{\sum_{i=1}^{m}\sum_{j=1}^{n}[X(i,j) - O(i,j)]^2}{\sum_{i=1}^{m}\sum_{j=1}^{n}[F(i,j) - O(i,j)]^2} \tag{23}$$

here, X represents the noise image, F represents the filtered image, and O represents the original image.

The dynamic range of IQI is $[-1, 1]$. The best value 1 is achieved if and only if the reconstructed image is equal to the noise-free image. Whereas, The lowest value of -1 occurs when the reconstructed image is twice the mean of the noise-free image subtracted by that of the noise-free image. This quality index models any distortion as a combination of three factors: loss of correlation, mean distortion, and contrast distortion. The calculation formula is as follows.

$$IQI = \frac{4\delta_{xy}\bar{x}\bar{y}}{\left(\delta_x^2 + \delta_y^2\right)\left[(\bar{x})^2 + (\bar{y})^2\right]} \tag{24}$$

where x is the noise-free image, y is the reconstructed image, $\bar{x}$ and $\bar{y}$ are the mean value of the noise-free image and the reconstructed image, δ_x^2 and δ_y^2 are the variances of the noise-free image and the reconstructed image, δ_{xy} is the covariance of x and y.

As in the previous ablation experiment, PSNR and SSIM are still used to describe the objective evaluation of various competitive algorithms. As shown in Table 3, from the test results, it can be seen that the LCMF-TV algorithm proposed in this paper obtains the best results on the values of MSE, PSNR, SSIM, IEF, and IQI among the listed competitive algorithms for spatial target images in long exposure mode. The proposed algorithm has superior performance in linear correlation, average similarity, and contrast similarity, which is beneficial for subsequent image processing.

To make the experiment more convincing, we increased the number of test images. We conducted algorithm comparison experiments with 20 simulated images and plotted PSNR and SSIM curves. As shown in Figure 9.

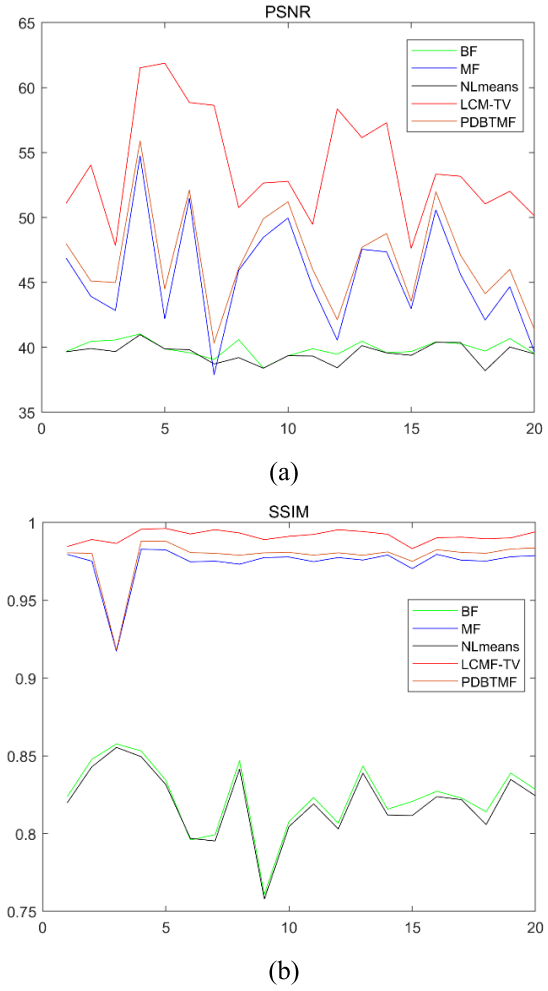

FIGURE 9. (a) PSNR curve of simulated images. (b) SSIM curve of simulated images.

From the curve graph, it can be seen that the method proposed in this article outperforms the competitive algorithm in various indicators when processing long-exposure images of the wide-field imaging system. Meanwhile, multiple sets of experimental results have also demonstrated the stability of the algorithm proposed in this article.

B. REAL IMAGES

In this section, we will use real spatial target images to visually compare the processing results of various competitive algorithms and our algorithm.

The real image data used in this article is all collected by a certain type of wide-field surveillance system. The system needs to complete relevant verification tests on the ground before being launched into space. The real image data was

TABLE 3. Objective evaluation results of five sets of simulated image processing.

		MF	BF	NL-means	PDBTMF	LCMF-TV
Image1	PSNR	44.5726	40.9052	40.2684	45.3254	53.6521
	SSIM	0.9746	0.8502	0.8492	0.9778	0.9928
	MSE	9.3694×10^{3}	2.1791×10^{4}	2.5232×10^{4}	7.3291×10^{3}	1.1577×10^{3}
	IEF	3.1992	1.0757	0.9503	4.2298	25.8891
	IQI	0.7126	0.5527	0.5078	0.7854	0.9669
Image2	PSNR	40.6475	40.1202	38.9218	41.8934	51.7484
	SSIM	0.9775	0.8173	0.8132	0.9800	0.9882
	MSE	2.3123×10^{4}	2.6108×10^{4}	3.4404×10^{4}	9.4903×10^{3}	1.7945×10^{3}
	IEF	1.3587	1.0712	0.8360	2.7865	118.5326
	IQI	0.6502	0.6705	0.5841	0.7189	0.9578
Image3	PSNR	47.5910	39.9749	40.0125	49.2387	54.4678
	SSIM	0.9770	0.8270	0.8256	0.9791	0.9912
	MSE	4.6740×10^{3}	2.6996×10^{4}	2.6763×10^{4}	4.8798×10^{3}	9.5943×10^{2}
	IEF	5.8667	1.0718	1.0995	7.7754	46.8958
	IQI	0.7412	0.7780	0.7778	0.8012	0.9711
Image4	PSNR	47.4809	39.5786	39.5560	47.9891	53.6956
	SSIM	0.9803	0.8353	0.8312	0.9872	0.9918
	MSE	4.7940×10^{3}	2.9575×10^{4}	2.9729×10^{4}	4.0087×10^{3}	1.1461×10^{3}
	IEF	7.0369	1.0652	1.0634	7.9178	210.9819
	IQI	0.7778	0.9103	0.9005	0.8122	0.9943
Image5	PSNR	42.9942	40.1147	39.8786	44.1029	49.8959
	SSIM	0.9714	0.8375	0.8300	0.9773	0.9887
	MSE	1.3470×10^{4}	2.6141×10^{4}	2.7601×10^{4}	1.1090×10^{4}	2.7492×10^{3}
	IEF	2.4284	1.0684	1.0056	3.0024	14.2819
	IQI	0.6922	0.5656	0.3285	0.7084	0.9092

obtained from ground validation tests. This camera's optical system utilizes imaging technology with a fiber optic panel to achieve a large-scale field of view. The camera is assembled with 8 CMOS detectors, the number of pixels in a single CMOS chip is 6144 (V) × 6144 (H), and each pixel data consists of 14 bits. This camera has a large field of view and a long detection distance, and the astronomical images captured are relatively complex. The experimental images were captured in star tracking mode, using an equatorial instrument to counteract the impact of Earth's rotation, setting the integration time to 3 seconds.

The experimental schematic diagram is shown in Figure 10.

The real images captured based on the above experimental environment are shown in Figure 11(a). To facilitate the display of the algorithm's processing effect, the local area is enlarged, as the Figure 11(b). Figures (c) to (f) show the comparison results between three classic image background denoising algorithms and the algorithm proposed in this paper, including median filters (MF), bilateral filters (BF), and non-local mean filtering algorithms (NL Means).

From Figure 10(c), it can be seen that the median filtering algorithm effectively removes the hot pixels in the image and smooths the background. However, it also smooths the spatial targets, resulting in blurred edges of the targets.

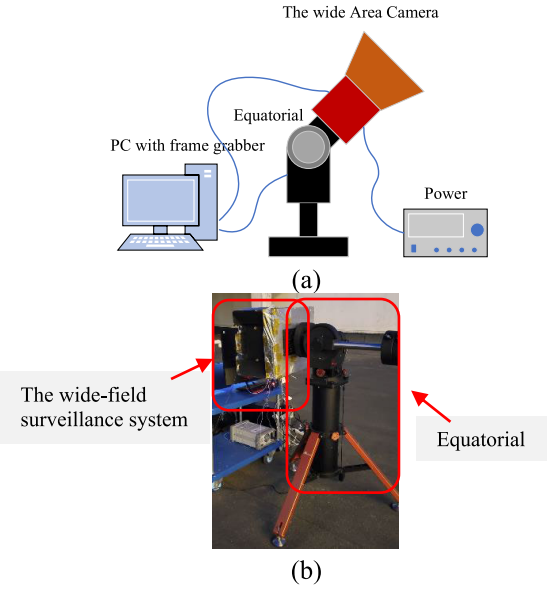

FIGURE 10. Schematic diagram of star tracking mode experiment.

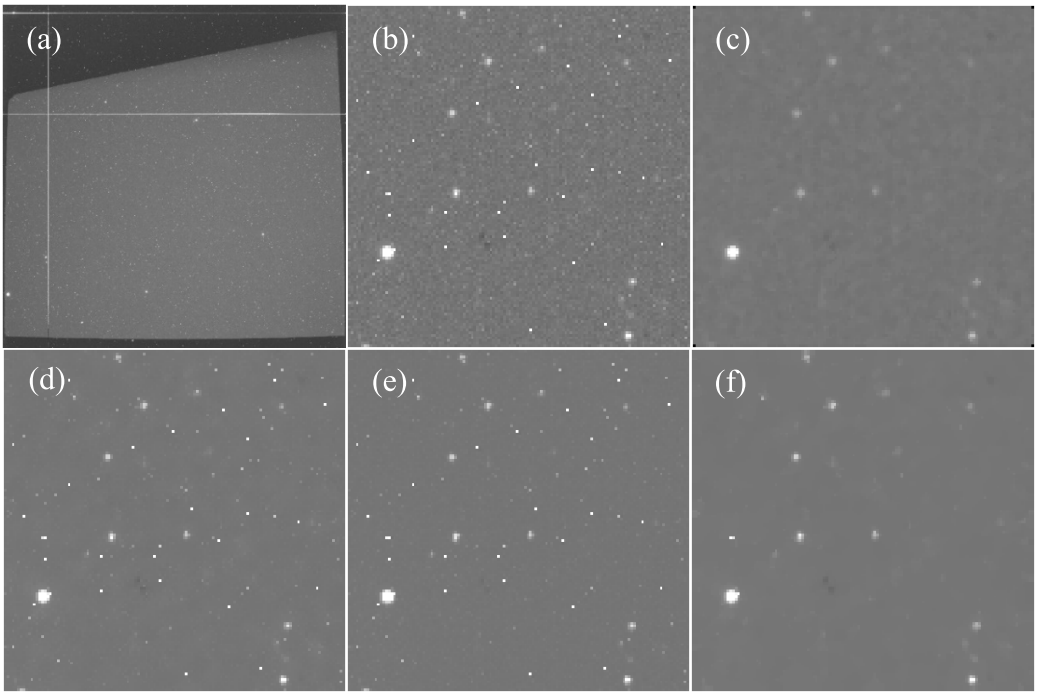

FIGURE 11. Comparison of processing effects of various competitive algorithms for real images. (a) Original image (6144 × 6144). (b) Local detail of the original image. (c) MF. (d) BF. (e) NL-means. (f) LCMF-TV.

TABLE 4. Running time of various methods. Units are seconds.

Size	MF	BF	NL-means	PDBTMF	LCMF-TV
512×512	0.0072	1.2259	24.8453	0.0085	1.2559

After algorithm processing, the non-uniformity of the image background in Figures 10(d) and (e) has been improved, and the edge information of spatial targets has been retained, but it cannot eliminate the hot pixels. Figure 10(f) shows the processing effect of the algorithm proposed in this paper. From the figure, spatial targets can be clearly identified, the image background is uniform, and the hot pixels are effectively removed.

C. RUNNING TIME

All test procedures are implemented in MATLAB on a desktop personal computer with an i7 2.8-GHz CPU and 16 GB RAM. By looking at the execution time of each method in Table 4, the LCMF-TV in this article does not have any advantages in running time, because the algorithm is a constrained optimized numerical calculation method that requires multiple iterations to achieve significant results.

D. DISCUSSION

In response to the imaging characteristics of long exposure in wide-field surveillance images, this article proposed an image denoising method based on local contrast and total variation model, which can be used for correcting non-uniform backgrounds. For such long-exposure images, the method proposed in this article outperforms other comparative methods in image denoising performance. Although the algorithm in this article has obvious advantages over other algorithms, it also requires a certain cost. Since the total variation model is a constrained optimization-type numerical algorithm, multiple iterations are required to obtain the optimal solution. Therefore, the execution time of this algorithm is slightly longer and is not suitable for scenarios with particularly high real-time requirements.

According to the above results and discussions, the amount of image data processed in this article is much smaller than that of real wide-field surveillance images. Therefore, future research should focus on solving non-uniform correction techniques for large fields of view and large data images. At the same time, it is crucial to improve the real-time performance of the algorithm and find a universal scene correction method suitable for various scenarios.

V. CONCLUSION

The main purpose of a space-wide-field surveillance system is to detect and locate space targets, to measure the speed and orbit of interested targets, and to protect the safety of the space environment. To improve the ability to detect weak targets, long exposure times are often used to obtain more energy from the target. In this case, the hot pixels of the detector cannot be ignored, seriously affecting the imaging quality. At the same time, due to the prolonged operation of the detector, its temperature will rise, which

also makes the hot pixels unstable and the background noise obvious, the detector calibration parameters obtained from ground radiation calibration experiments are no longer applicable. Therefore, this article is based on this application environment and proposes a noise suppression algorithm for complex backgrounds for the long exposure mode of space cameras. This algorithm does not use any prior knowledge of the target and can automatically remove noise from images in long exposure mode. To suppress impulse noise such as the hot pixels in images, an improved adaptive maxi-mum filtering algorithm was designed based on the traditional local contrast algorithm, which protected target information from being lost and optimized pixels that were only attacked by impulse noise. The total variation algorithm is used to eliminate residual background noise, detector readout noise, and non-uniform response. The above steps greatly eliminate the impact of the hot pixels, background noise, detector readout noise, and uneven response on spatial targets. We conducted experiments on a large number of simulated images and original star maps. In the experiment, we used two indicators, PSNR and SSIM, to evaluate the effectiveness of the algorithm. Among them, PSNR reflects the algorithm's ability to suppress noise and non-uniform backgrounds, while SSIM reflects the degree of correlation before and after image processing. We analyzed both subjective and objective evaluations and found that the algorithm proposed in this paper has significant advantages over several competing algorithms for star maps captured in long exposure mode. The experimental results show that compared to noisy images, after processing with the algorithm in this paper, PSNR is improved by 28% and SSIM is improved by 41.1%.

Our next step is to optimize the algorithm for subsequent hardware implementation, while also attempting more noise suppression strategies to further improve the flexibility of the algorithm. In addition, we will further expand the application scenarios of the algorithm and improve its robustness.

REFERENCES

[1] K. F. Hussain, K. Thangavel, A. Gardi, and R. Sabatini, "Autonomous optical sensing for space-based space surveillance," in *Proc. IEEE Aerosp. Conf.*, Big Sky, MT, USA, Mar. 2023, pp. 1–9, doi: 10.1109/AERO55745.2023.10115786.

[2] T. Schildknecht, "Optical surveys for space debris," *Astron. Astrophys. Rev.*, vol. 14, no. 1, pp. 41–111, Jan. 2007, doi: 10.1007/s00159-006-0003-9.

[3] M. J. Holzinger and M. K. Jah, "Challenges and potential in space domain awareness," *J. Guid., Control, Dyn.*, vol. 41, no. 1, pp. 15–18, Jan. 2018, doi: 10.2514/1.G003483.

[4] R.-Y. Sun, J.-W. Zhan, C.-Y. Zhao, and X.-X. Zhang, "Algorithms and applications for detecting faint space debris in GEO," *Acta Astronautica*, vol. 110, pp. 9–17, May 2015, doi: 10.1016/j.actaastro.2015.01.001.

[5] E. M. Gaposchkin, C. von Braun, and J. Sharma, "Space-based space surveillance with the space-based visible," *J. Guid., Control, Dyn.*, vol. 23, no. 1, pp. 148–152, Jan. 2000, doi: 10.2514/2.4502.

[6] Y. Wang and E. Ientilucci, "A practical approach to Landsat 8 TIRS stray light correction using multi-sensor measurements," *Remote Sens.*, vol. 10, no. 4, p. 589, Apr. 2018, doi: 10.3390/rs10040589.

[7] G. H. Chapman, R. Thomas, Z. Koren, and I. Koren, "Empirical formula for rates of hot pixel defects based on pixel size, sensor area, and ISO," *Proc. SPIE*, vol. 8659, Feb. 2013, Art. no. 86590, doi: 10.1117/12.2005850.

[8] D. Liu, X. Wang, Y. Li, Z. Xu, J. Wang, and Z. Mao, "Space target detection in optical image sequences for wide-field surveillance," *Int. J. Remote Sens.*, vol. 41, no. 20, pp. 7846–7867, Oct. 2020, doi: 10.1080/01431161.2020.1782508.

[9] Z. Xu, D. Liu, C. Yan, and C. Hu, "Stray light nonuniform background correction for a wide-field surveillance system," *Appl. Opt.*, vol. 59, no. 34, p. 10719, Dec. 2020, doi: 10.1364/ao.404685.

[10] T. Zhang, X. Li, J. Li, and Z. Xu, "CMOS fixed pattern noise elimination based on sparse unidirectional hybrid total variation," *Sensors*, vol. 20, no. 19, p. 5567, Sep. 2020, doi: 10.3390/s20195567.

[11] W. Huawei, M. Caiwen, C. Jianzhong, and Z. Haifeng, "An adaptive two-point non-uniformity correction algorithm based on shutter and its implementation," in *Proc. 5th Int. Conf. Measuring Technol. Mechatronics Autom.*, Hong Kong, Jan. 2013, pp. 174–177, doi: 10.1109/ICMTMA.2013.51.

[12] S.-X. Xing, J. Zhang, L. Sun, B.-K. Chang, and Y.-S. Qian, "Two-point nonuniformity correction based on LMS," *Proc. SPIE*, vol. 5640, p. 130, Jan. 2005, doi: 10.1117/12.566145.

[13] M. E. Feinholz, S. J. Flora, S. W. Brown, Y. Zong, K. R. Lykke, M. A. Yarbrough, B. C. Johnson, and D. K. Clark, "Stray light correction algorithm for multichannel hyperspectral spectrographs," *Appl. Opt.*, vol. 51, no. 16, p. 3631, Jun. 2012, doi: 10.1364/ao.51.003631.

[14] A. Khmag, "Natural digital image mixed noise removal using regularization Perona–Malik model and pulse coupled neural networks," *Soft Comput.*, vol. 27, no. 21, pp. 15523–15532, Nov. 2023, doi: 10.1007/s00500-023-09148-y.

[15] A. Khmag, "Additive Gaussian noise removal based on generative adversarial network model and semi-soft thresholding approach," *Multimedia Tools Appl.*, vol. 82, no. 5, pp. 7757–7777, Feb. 2023, doi: 10.1007/s11042-022-13569-6.

[16] G. Strang, "Wavelet transforms versus Fourier transforms," *Bull. Amer. Math. Soc.*, vol. 28, no. 2, pp. 288–305, 1993, doi: 10.1090/s0273-0979-1993-00390-2.

[17] A. Mustafi and S. K. Ghorai, "A novel blind source separation technique using fractional Fourier transform for denoising medical images," *Optik*, vol. 124, no. 3, pp. 265–271, Feb. 2013, doi: 10.1016/j.ijleo.2011.11.052.

[18] S. Veerasingam, M. Ranjani, R. Venkatachalapathy, A. Bagaev, V. Mukhanov, D. Litvinyuk, M. Mugilarasan, K. Gurumoorthi, L. Guganathan, V. M. Aboobacker, and P. Vethamony, "Contributions of Fourier transform infrared spectroscopy in microplastic pollution research: A review," *Crit. Rev. Environ. Sci. Technol.*, vol. 51, no. 22, pp. 2681–2743, Nov. 2021, doi: 10.1080/10643389.2020.1807450.

[19] Z. Lin, C. Tian, Y. Hou, and W. X. Zhao, "Improving graph collaborative filtering with neighborhood-enriched contrastive learning," in *Proc. ACM Web Conf.*, Apr. 2022, pp. 2320–2329, doi: 10.1145/3485447.3512104.

[20] A. Shah, J. I. Bangash, A. W. Khan, I. Ahmed, A. Khan, A. Khan, and A. Khan, "Comparative analysis of median filter and its variants for removal of impulse noise from gray scale images," *J. King Saud Univ. Comput. Inf. Sci.*, vol. 34, no. 3, pp. 505–519, Mar. 2022, doi: 10.1016/j.jksuci.2020.03.007.

[21] E. J. Leavline and D. A. A. G. Singh, "Salt and pepper noise detection and removal in gray scale images: An experimental analysis," *Int. J. Signal Process., Image Process. Pattern Recognit.*, vol. 6, no. 5, pp. 343–352, Oct. 2013, doi: 10.14257/ijsip.2013.6.5.30.

[22] S. H. Teoh and H. Ibrahim, "Median filtering frameworks for reducing impulse noise from grayscale digital images: A literature survey," *Int. J. Future Comput. Commun.*, vol. 1, no. 4, pp. 323–326, 2012, doi: 10.7763/ijfcc.2012.v1.87.

[23] M. Elad, "On the origin of the bilateral filter and ways to improve it," *IEEE Trans. Image Process.*, vol. 11, no. 10, pp. 1141–1151, Oct. 2002, doi: 10.1109/TIP.2002.801126.

[24] C. Tomasi and R. Manduchi, "Bilateral filtering for gray and color images," in *Proc. 6th Int. Conf. Comput. Vis.*, Bombay, India, Jan. 1998, pp. 839–846, doi: 10.1109/ICCV.1998.710815.

[25] C. Sutour, C.-A. Deledalle, and J.-F. Aujol, "Adaptive regularization of the NL-Means: Application to image and video denoising," *IEEE Trans. Image Process.*, vol. 23, no. 8, pp. 3506–3521, Aug. 2014, doi: 10.1109/TIP.2014.2329448.

[26] Y. Chen, W. Cao, L. Pang, and X. Cao, "Hyperspectral image denoising with weighted nonlocal low-rank model and adaptive total variation regularization," *IEEE Trans. Geosci. Remote Sens.*, vol. 60, pp. 1–15, 2022, Art. no. 5544115, doi: 10.1109/TGRS.2022.3214542.

[27] G. E. Healey and R. Kondepudy, "Radiometric CCD camera calibration and noise estimation," *IEEE Trans. Pattern Anal. Mach. Intell.*, vol. 16, no. 3, pp. 267–276, Mar. 1994, doi: 10.1109/34.276126.
[28] P. Jiang, C. Liu, W. Yang, Z. Kang, and Z. Li, "Automatic space debris extraction channel based on large field of view photoelectric detection system," *Publications Astronomical Soc. Pacific*, vol. 134, no. 1032, Feb. 2022, Art. no. 024503, doi: 10.1088/1538-3873/ac4c9d.
[29] R. Liu, D. Wang, D. Zhou, and P. Jia, "Point target detection based on multiscale morphological filtering and an energy concentration criterion," *Appl. Opt.*, vol. 56, no. 24, p. 6796, Aug. 2017, doi: 10.1364/ao.56.006796.
[30] N. V. Loukianova, H. O. Folkerts, J. P. V. Maas, D. W. E. Verbugt, A. J. Mierop, W. Hoekstra, E. Roks, and A. J. P. Theuwissen, "Leakage current modeling of test structures for characterization of dark current in CMOS image sensors," *IEEE Trans. Electron Devices*, vol. 50, no. 1, pp. 77–83, Jan. 2003, doi: 10.1109/TED.2002.807249.
[31] C. L. P. Chen, H. Li, Y. Wei, T. Xia, and Y. Y. Tang, "A local contrast method for small infrared target detection," *IEEE Trans. Geosci. Remote Sens.*, vol. 52, no. 1, pp. 574–581, Jan. 2014, doi: 10.1109/TGRS.2013.2242477.
[32] Y. Chang, H. Fang, L. Yan, and H. Liu, "Robust destriping method with unidirectional total variation and framelet regularization," *Opt. Exp.*, vol. 21, no. 20, p. 23307, Sep. 2013, doi: 10.1364/OE.21.023307.
[33] L. I. Rudin, S. Osher, and E. Fatemi, "Nonlinear total variation based noise removal algorithms," *Phys. D, Nonlinear Phenomena*, vol. 60, nos. 1–4, pp. 259–268, Nov. 1992, doi: 10.1016/0167-2789(92)90242-F.
[34] T. F. Chan, H. M. Zhou, and R. H. Chan, "Continuation method for total variation denoising problems," *Proc. SPIE*, vol. 2563, pp. 314–325, Jun. 1995, doi: 10.1117/12.211408.
[35] H. Masood, A. Zafar, M. U. Ali, T. Hussain, M. A. Khan, U. Tariq, and R. Damaševič ius, "Tracking of a fixed-shape moving object based on the gradient descent method," *Sensors*, vol. 22, no. 3, p. 1098, Jan. 2022, doi: 10.3390/s22031098.
[36] B. R. Jana, H. Thotakura, A. Baliyan, M. Sankararao, R. G. Deshmukh, and S. R. Karanam, "Pixel density based trimmed median filter for removal of noise from surface image," *Appl. Nanoscience*, vol. 13, no. 2, pp. 1017–1028, Feb. 2023, doi: 10.1007/s13204-021-01950-0.
[37] A. Khmag, A. R. Ramli, S. A. R. Al-haddad, and N. Kamarudin, "Natural image noise level estimation based on local statistics for blind noise reduction," *Vis. Comput.*, vol. 34, no. 4, pp. 575–587, Apr. 2018, doi: 10.1007/s00371-017-1362-0.

PENGJI ZHOU was born in Yichun, Heilongjiang, China, in 1985. He received the B.S. degree in measurement and control technology and instrumentation and the M.S. degree in measuring and testing technologies and instruments from the University of Electronic Science and Technology of China, Chengdu, China, in 2008 and 2013, respectively. He is currently pursuing the Ph.D. degree with the Changchun Institute of Optics, Fine Mechanics and Physics, Chinese Academy of Sciences, Changchun, China.

He is currently an Assistant Researcher with the Changchun Institute of Optics, Fine Mechanics and Physics, Chinese Academy of Sciences. His research interests include image processing, weak target detection, and computer vision.

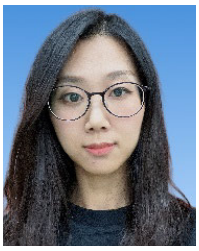

DI WU was born in Changchun, Jilin, China, in 1988. She received the B.S. degree in electronic and information engineering and the M.S. degree in circuits and systems from Jilin University, Changchun, in 2011 and 2014, respectively, and the Ph.D. degree in mechanical electronics engineering from the Changchun Institute of Optics, Fine Mechanics and Physics, Chinese Academy of Sciences, Changchun, in 2023.

She is currently an Assistant Researcher with the Chinese Academy of Sciences. Her research interests include image processing, target radiation characteristics, weak target detection, and computer vision.

XIAODONG WANG was born in Jilin, China, in 1970. He received the Ph.D. degree in optical engineering from the Changchun Institute of Optics, Fine Mechanics and Physics, Chinese Academy of Sciences, Changchun, China, in 2003.

He is currently a Researcher with the Changchun Institute of Optics, Fine Mechanics and Physics, Chinese Academy of Sciences. His research interests include space optical remote sensing imaging and information processing technology.

CHANGXIANG YAN was born in Honghu, Hubei, China, in 1973. He received the M.S. degree in engineering from Zhejiang University, Zhejiang, China, in 1998, and the Ph.D. degree from the Changchun Institute of Optics, Fine Mechanics and Physics, Chinese Academy of Sciences, Changchun, China, in 2001.

Since 2010, he has been the Director of the Space Optics Laboratory, Changchun Institute of Optics, Fine Mechanics and Physics, Chinese Academy of Sciences. His research interests include opto-mechatronics technology for space optical remote sensing instruments, multispectral and hyperspectral spatial remote sensing imaging, polarization detection, and space surveillance.

DALI ZHOU was born in Changchun, Jilin, China, in 1989. He received the B.S. degree in electronic information science and technology and the M.S. degree in circuits and systems from Northeast Normal University, Changchun, in 2013 and 2016, respectively.

He is currently an Assistant Researcher with the Changchun Institute of Optics, Fine Mechanics and Physics, Chinese Academy of Sciences. His research interests include image processing, faint target detection, and computer vision.